Revealing the Charge Density Wave Proximity Effect in Graphene on 1T-TaS_2

Michael A. Altvater[1+], Sheng-Hsiung Hung[2+], Nikhil Tilak[1], Choong-Jae Won[3], Guohong Li[1], Sang-Wook Cheong[1], Chung-Hou Chung[4,5*], Horng-Tay Jeng[2,5*] and Eva Y. Andrei[1*]

[1] Department of Physics and Astronomy, Rutgers, the State University of New Jersey, 136 Frelinghuysen Rd, Piscataway, New Jersey 08854, USA
[2] Department of Physics, National Tsing-Hua University, 101 Guangfu Road, Hsinchu 30013, Taiwan
[3] Laboratory for Pohang Emergent Materials and Max Plank POSTECH Center for Complex Phase Materials, Department of Physics, Pohang University of Science and Technology, Pohang 37673, Korea
[4] National Chiao Tung University, 1001 Daxue Road, Hsinchu 30010, Taiwan
[5]Physics Division, National Center for Theoretical Sciences, Taipei 10617, Taiwan

*Corresponding authors E-mail: chung0523@nycu.edu.tw, jeng@phys.nthu.edu.tw, eandrei@physics.rutgers.edu
[+]Equal contributors

The proximity-effect, a phenomenon whereby materials appropriate each other's electronic-properties, is widely used in nano-scale devices to induce electron-correlations at heterostructure interfaces. Commonly observed proximity-induced correlation-effects include superconductivity, magnetism, and spin-orbit interactions. Thus far however proximity-induced charge density waves (CDW) were not realized, primarily because of screening in 3D metals and defect scattering at interfaces. Here we report the observation of a proximity-induced CDW made possible by employing 2D-materials with pristine and atomically smooth surfaces. Using scanning-tunneling microscopy (STM) and spectroscopy (STS) together with theoretical-modeling to probe the interface between graphene and a 1T-TaS_2 crystal, we show that interactions induce a CDW within graphene and modify the band structure at the surface of 1T-TaS_2. We further show that the mechanism underlying the proximity-induced CDW is driven by short-range exchange interactions that are distinctly different from previously observed proximity-effects.

The isolation and manipulation of atomically thin layered materials provides a ready-made two dimensional electron system [1] whose properties can be tuned by external knobs, such as stress or substrate morphology [2-4], leading to the emergence of correlated electron phases. Distinct from these external knobs, a very powerful approach to manipulate electron correlations in these materials is by contact proximity effects. It is well known that proximitizing materials that host correlated electron phases, such as superconductivity [5] or magnetism [6], with normal metals, induces correlations in the normal metal. These effects are a direct consequence of the quantum mechanical properties of electrons in solids; specifically, the non-local nature of electrons. As quantum particles do not have a well-defined position, electronic states cannot abruptly change from one type of ordering to another at the interface of two materials. Consequently, correlated states persist into the normal metal where scattering events begin to destroy the coherence (and vice versa). In the case of 2D materials where scattering is reduced due to their atomically sharp interfaces, proximity-effects are particularly robust allowing correlated states to persist over long distances. The discovery of graphene and other 2D materials, together with the technology enabling 2D heterostructures has led to the observation of strong proximity effects at the atomic limit including proximity induced superconductivity, magnetism and spin-orbit effects [7-15].

The CDW is yet another quantum many-body state arising from electron correlations, such as on-site Coulomb repulsion and short-ranged anti-ferromagnetic spin-exchange interactions., that is seen in correlated insulators and unconventional superconductors [16] as well as in 2D transition-metal dichalcogenide (TMDs) [17]. However, inducing a proximity effect between a CDW material and a normal metal has remained elusive. This is primarily due to screening in 3D metals and interface defect scattering. As described below, the use of 2D materials that were stacked in an inert atmosphere to avoid interface damage and contamination, together with sensitive local probes providing direct access to the charge distribution in graphene, made it possible to overcome these hurdles.

In this work, we present microscopic evidence of the proximity effect between the CDW material 1T-TaS_2, and graphene. Through scanning tunneling microscopy (STM) and spectroscopy (STS), we show that the charge density modulation in 1T-TaS_2 persists within the contacted graphene layer. By comparing with first-principles calculations based on density-functional theory (DFT), we find that in addition to a global charge-transfer between the two surfaces caused by the relative electron negativity, the proximity induced CDW in graphene is driven by a novel mechanism of short-range exchange interactions mediated by second-order local electron hopping, which is distinctly different from superconducting, magnetic, and spin-orbit proximity effects.

1T-TaS_2 is known to exhibit a strongly coupled, commensurate CDW below ~180K involving 13 unit cells where 12 of 13 Ta atoms displace from their high-temperature, equilibrium positions toward the central, 13th Ta atom[18-22]. . This lattice displacement and corresponding charge density modulation repeat periodically within each layer to form a triangular super-lattice with period of $\sqrt{13}$ unit cells of 1T-TaS_2. Fig. 1(a) left panel shows the $\sqrt{13} \times \sqrt{13}$ CDW reconstructed 1T-TaS_2 supercell. As shown in Fig. S3, the origin of the CDW formation in 1T-TaS_2 is the Kohn anomaly in the acoustic branch of the phonon spectrum along the Γ→M direction with the phonon frequency critically suppressed by electron-phonon interaction [23,24], leading to the static displacement of the lattice with the wavevector $\mathbf{Q_{CDW}}$ corresponding to the $\sqrt{13} \times \sqrt{13}$ CDW reconstruction. This soft phonon mode at the Kohn anomaly wavevector $\mathbf{Q_{CDW}}$ consists primarily of longitudinal vibrations of Ta atoms with a minor contribution from transverse vibrations of S atoms relative to the phonon propagating direction $\mathbf{Q_{CDW}}$. The star-of-David atomic arrangement involves the local lattice contraction around the center of the star, in which the bond lengths between Ta ions are shorter than those between Ta ions outside the star. To compare with STM images, we calculated the partial charge density of the two lowest energy bands as shown in Fig. 1(a) right panel. The electron cloud mainly distributes over the stars with the highest charge density enhancement of ~5x10^{-3} e/Å^3 locating at the center Ta ion of the star.

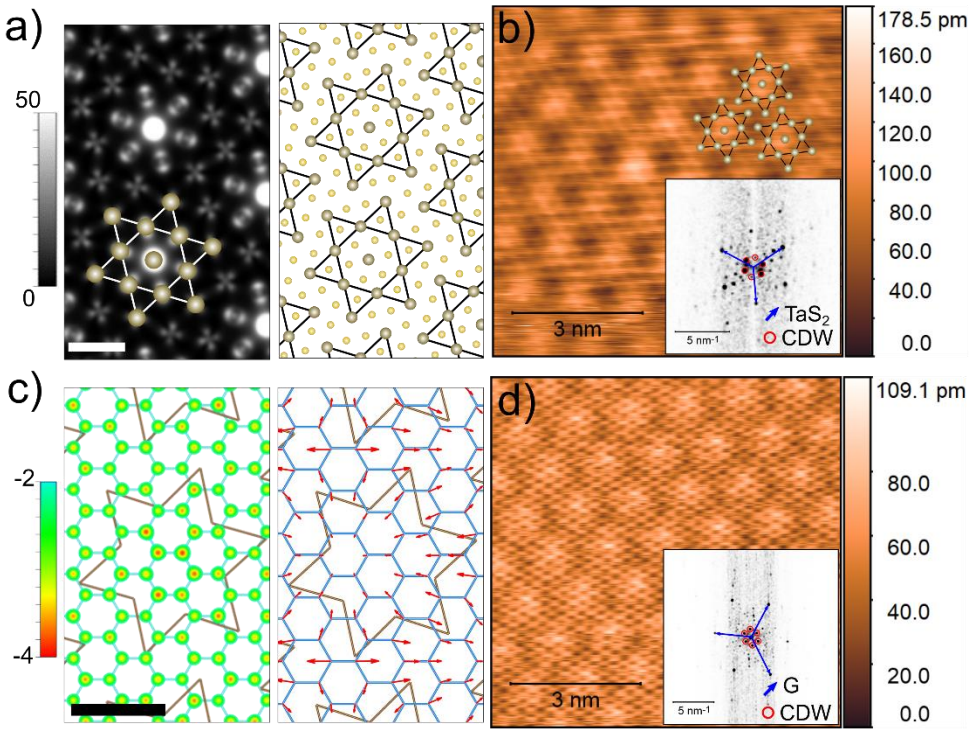

Figure 1 STM Topography of Bare and Encapsulated 1T-TaS2: a) Left panel: DFT computed charge density of the two lowest energy bands in the commensurate CDW in 1T-TaS_2. Scale bar is 5Å. Color scale units are 10^{-4}e/ Å^3. Right panel: Ball and stick model of the $\sqrt{13} \times \sqrt{13}$ CDW reconstructed 1T-TaS_2 lattice with David star clusters outlined. b) STM topography of bare surface of 1T-TaS_2 shows the CDW charge modulation as well as the atomic lattice of the 1T-TaS_2 top layer (Ta positions marked with beige dots) (V_b=1.2V, I_{SP}=40pA) inset: FFT of topography image shows Bragg peaks from the lattice as well as the CDW modulation. c) Left panel: DFT computed charge transfer of the graphene layer (the charge density of pristine graphene is subtracted from the charge density of the graphene layer on 1T-TaS_2) shows a local modulation of doping with the periodicity of the CDW in TaS_2. The pattern of the colored dots indicate stronger hole doping in graphene within the David stars (highlighted in brown). Scale bar is 5Å. Color scale units are 10^{-4}e/ Å^3. Right panel: Blue honeycomb and brown stars indicate the graphene lattice and 1T-TaS_2 David star, respectively. The red arrows demonstrate the displacements of carbon atoms given from DFT geometrical optimization. The maximum displacement is approx. 0.001Å. Most graphene atoms distort toward the center of the David star of the 1T-TaS_2 CDW forming the proximity induced CDW in graphene. d) STM topography of graphene placed on 1T-TaS_2 shows both the graphene lattice as well as the super-lattice charge density modulation associated with the CDW of 1T-TaS_2 inset: FFT of topography image shows Bragg peaks from the graphene lattice as well as the CDW modulation.

Experimentally, the charge density modulation is evident in the STM topography image of the bare 1T-TaS_2 surface, Fig. 1(b). The STM measures both the density of states (DOS) modulation due to the CDW reconstruction and the positions of the sulfur sub-lattice. This can be seen in the fast Fourier transform (FFT) [Fig. 1(b) inset] which shows Bragg peaks associated with the 1T-TaS_2 lattice spacing (blue arrows) as well as peaks corresponding to the CDW wavevectors (red circles). The $\sqrt{13} \times \sqrt{13}$ CDW reconstruction is depicted as star-shaped clusters of Ta atoms in Fig. 1(b).

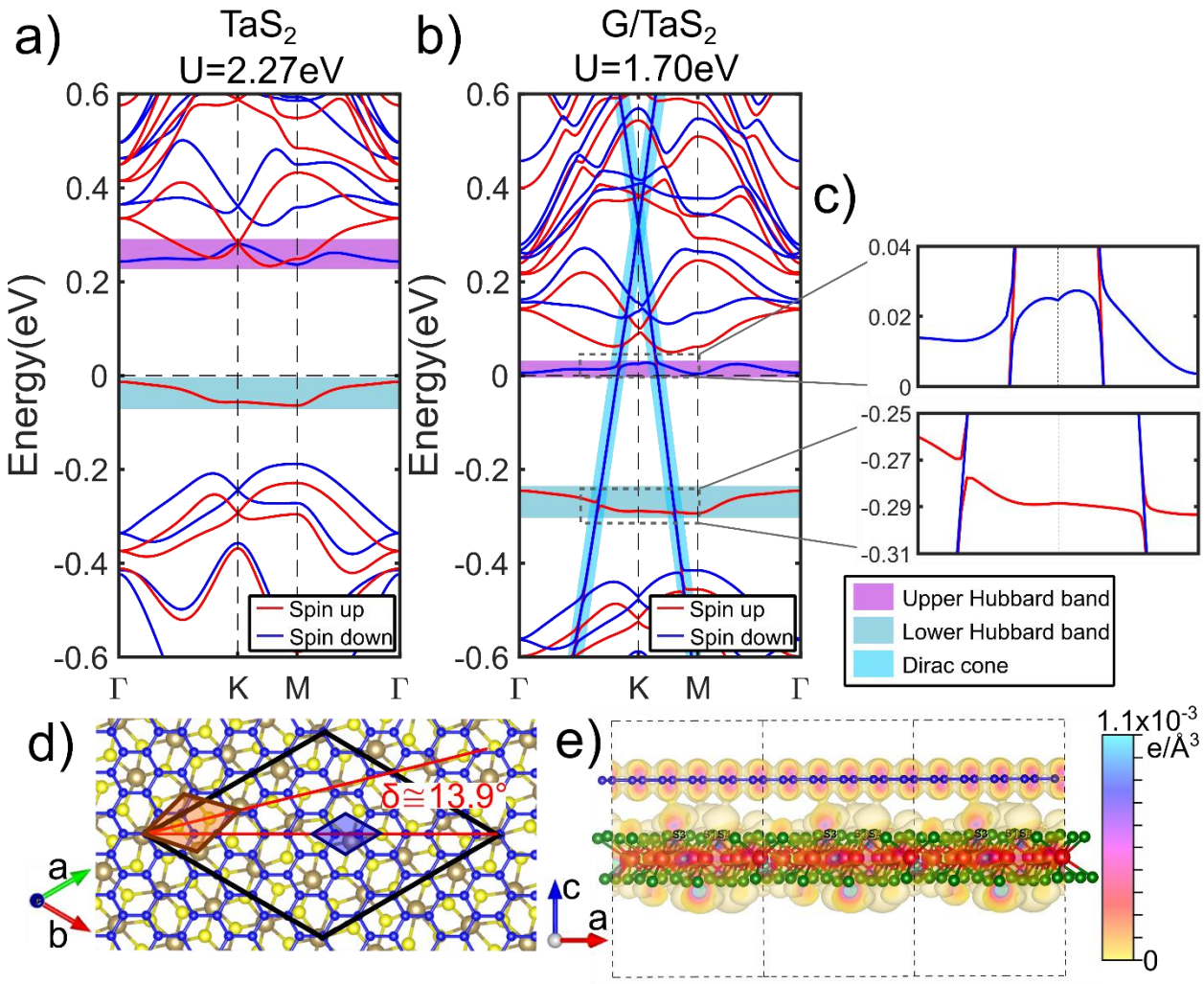

Figure 2: Band Structureof 1T-TaS2 and G/TaS$_2$ a) GGA+U band structure of $\sqrt{13} \times \sqrt{13}$CDW reconstructed 1T-TaS$_2$ with U=2.27eV. Hubbard bands, associated with the localized electronic state at the center of the David stars, are highlighted. b) GGA+U band structure of G/TaS$_2$ using a phenomenological value U=1.70eV. Owing to the charge transfer from graphene to 1T-TaS$_2$, the Fermi level (zero energy) moves from the lower Hubbard band to the upper Hubbard band, and the graphene-associated Dirac point at the K-point of the superstructure Brillouin zone is shifted to ~ 0.3eV above the Fermi level (E_F) indicating hole doping. The hole distribution [Fig. 1(c)] forms the real space modulation in graphene with the same periodicity as the underlying √13×√13 CDW of 1T-TaS$_2$ through the proximity effect. Hubbard bands and Dirac cone are highlighted for clarity. c) Zoomed in view of the crossing points between the Dirac cone and Upper (top) and Lower (bottom) Hubbard bands. d) Top view of G/TaS$_2$ heterostructure. Blue, brown, and yellow spheres indicate C, Ta, and S atoms, respectively. Black, blue, and brown rhombuses show the 5x5 G/$\sqrt{13} \times \sqrt{13}TaS_2$ supercell, graphene 1x1 unit cell, and 1T-TaS$_2$ 1x1 unit cell, respectively. The graphene and TaS$_2$ layer are twisted by ~13.9° in this CDW phase. e) Side view of G/TaS$_2$ heterostructure overlaid with the charge density map (bubble-shaped color contour indicating the electron density) corresponding to the states at the two crossing points of the Dirac cone and Lower Hubbard band. The slight overlap between graphene and 1T-TaS$_2$ electron clouds give rise to

the interlayer coupling and proximity effect. Here, blue, red, and green spheres represent C, Ta, and S atoms, respectively.

First-principle electronic structure calculations were performed using the projector augmented wave (PAW) approach within the framework of density functional theory (DFT) as implemented in the Vienna ab initio Simulation Package (VASP) [25-28]. The exchange-correlation is described in the Perdew-Burke-Ernzerhof (PBE) form of generalized gradient approximation (GGA) [28,29]. A side view of the graphene/TaS_2 (G/TaS_2) heterostructure used in the DFT calculation is shown in Fig. 2(d). By subtracting the calculated charge density of freestanding graphene monolayer from the charge density of G/TaS_2, Fig. 1(c) left panel illustrates the 1T-TaS_2 induced local doping in the graphene cover layer. From the induced charge density map, we observe a negative induced charge density of ~0.0004 holes/ $Å^3$ near the centers of the David stars in the 1T-TaS_2 layer below (local hole doping). The induced charge density modulation in the graphene layer shows the same periodicity as the CDW in 1T-TaS_2 layer with the strongest charge transfer located around the center of the 1T-TaS_2 CDW stars with the strongest CDW potential, demonstrating the correlation between graphene and 1T-TaS_2. Indeed, STM topography measurements of the top graphene layer in a G/TaS_2 heterostructure also reveal a strong intensity modulation of graphene's honeycomb lattice with a period that matches that of the CDW in 1T-TaS_2 [see Fig. 1(d)]. The two-dimensional periodic modulation is evident in the fast Fourier transform (FFT) of the topography image [Fig. 1(d) inset]. As detailed below, the charge transfer in graphene layer provides clear evidence of the CDW proximity effect.

The induced charge modulation in the graphene layer [Fig. 1c] is accompanied by a periodic lattice distortion in the graphene lattice. Due to the strong carbon-carbon bonds and relatively weak interlayer coupling between graphene and 1T-TaS_2 layers, the lattice distortion is very small (<0.001Å) so that it cannot be seen in Fig. 1c, left panel. In the right panel of Fig. 1c, we demonstrate the graphene lattice distortion by attaching a red arrow at each carbon atom indicating the atomic displacement given from DFT lattice relaxation calculations. Similar to the David star formation in the 1T-TaS_2 layer, all carbon atoms shift toward the center of the CDW star, forming the proximity induced CDW in graphene. Such small lattice displacement cannot be detected in the STM topography measurement [Fig. 1d].

To investigate the charge transfer between the two materials at the interface, we calculate the band structure of bare 1T-TaS_2 using the lattice-relaxed $\sqrt{13} \times \sqrt{13}$ CDW supercell as well as the G/TaS_2 heterostructure by placing 5x5 unit cells of graphene on top. The top and side views of the G/TaS_2 lattice model are depicted in Figs. 2(d) and (e), respectively. To take the strong correlation of Ta d-electrons into consideration, we perform generalized-gradient approximation plus on-site U (GGA+U) calculations with U=2.27eV for bare, monolayer 1T-TaS_2 in accordance with previous DFT calculations [30,31] as shown in Fig. 2(a). The CDW-induced isolated half-filled spin-degenerate flat band at E_F [see Fig. S4] splits into occupied spin up lower Hubbard band (LHB) and empty spin down upper Hubbard band (UHB) with a Mott gap of ~0.25eV in between. The on-site Hubbard U significantly enhances the Mott gap from ~0.12eV [see Fig. S5] to ~0.25eV [Fig. 2(a)] so that the UHB touches the lowest conduction bands, while experiments observe a localized Hubbard band more separated from the conduction band. This discrepancy implies the on-site Hubbard U of 2.27eV might be somewhat overestimated. Possible reasons are discussed below.

In the band structure of the G/TaS_2 heterostructure, both the 1T-TaS_2 Hubbard bands and the graphene Dirac cone are preserved [see Fig. 2(b)]. Compared to bare 1T-TaS_2, the Fermi level moves

from the LHB up to the UHB due to the charge transfer from graphene to 1T-TaS_2. This is also accompanied with an energy shift of the graphene Dirac point from the Femi level E_F up to ~0.3eV above E_F at the K-point of the superstructure Brillouin zone [Fig. S3]. A careful comparison of the Dirac cone of G/TaS_2 with that of bare graphene leads us to conclude that the Fermi velocity is not changed by the proximity to 1T-TaS_2. The highly dispersive p_z-orbital derived Dirac cone intersects the CDW and Mott gaps and crosses both the dz^2-orbital derived narrow LHB and UHB. They indeed interact with each other, though in a gentle manner. Four small gaps of order 10meV emerge at the four crossing points as shown in the insets of Fig. 2(c). These small gaps which originate from the weak interlayer couplings indicate finite hybridization between the Dirac and Hubbard states, giving rise to the proximity effect between graphene and 1T-TaS_2 as illustrated in Fig. 2(e).

Graphene is known to be a wide bandwidth semi-metal with high-mobility itinerant carriers. With graphene on top of 1T-TaS_2, there exists nontrivial charge transfer from graphene to 1T-TaS_2, as shown in the LDSA+U band structure in Fig. 2(b). These highly mobile electrons from graphene somewhat suppress the localized picture of the narrow Hubbard d-bands in 1T-TaS_2 and thus reduce the on-site U value of Ta. A comparison of the band structures for different U values with the STS results, suggests that the graphene layer screens the Coulomb interaction in 1T-TaS_2 and the Hubbard U of Ta is lowered by ~0.5eV due to the itinerant electrons in graphene. Therefore, we show in Fig. 2(c) the G/TaS_2 the band structure with a phenomenological value U=1.70eV, which reasonably reproduces the trend observed in the STS measurements (below).

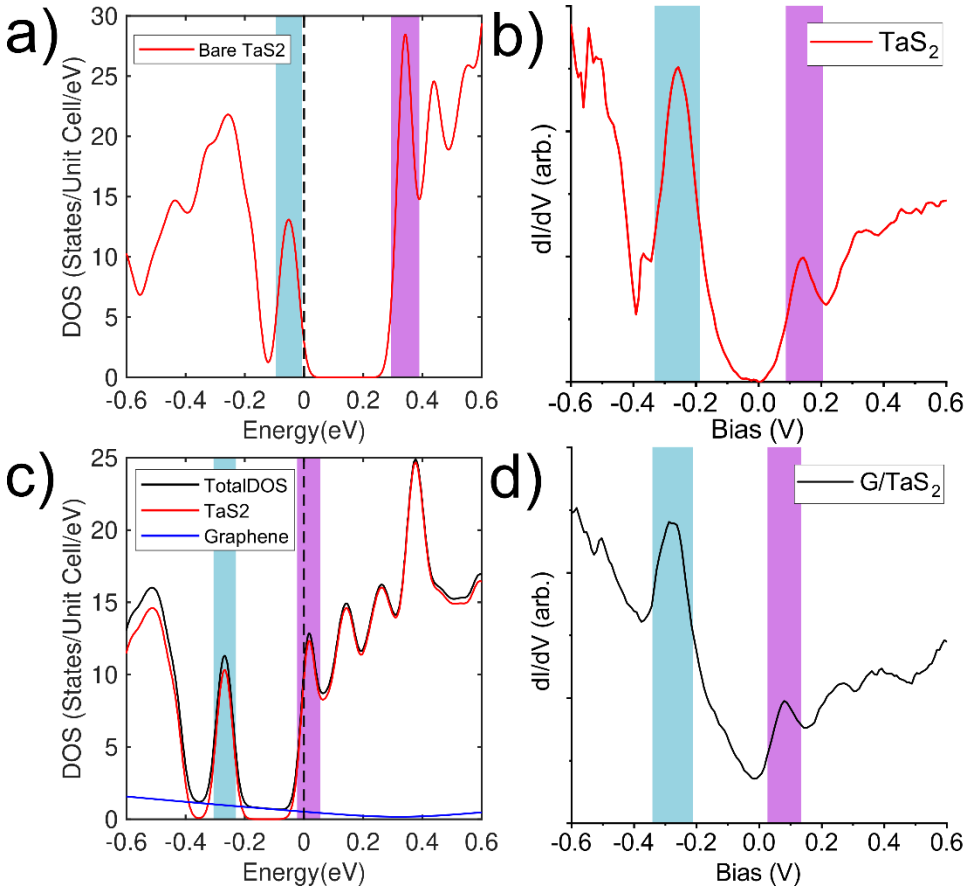

Figure 3: Density of States of Bare 1T-TaS_2 and G/1T-TaS_2 a) GGA+U calculated DOS of bare 1T-TaS_2 (U=2.27eV) b) Measured tunneling spectroscopy (STS) of the bare 1T-TaS_2 surface shows a gap at zero bias with peaks associated with upper and lower Hubbard bands (highlighted with violet and blue, respectively) in agreement with the calculated result (a). c) GGA+U calculated DOS of the G/TaS_2 heterostructure showing features resembling the Hubbard bands, conduction band, and valence band of 1T-TaS_2 with a reduced Mott-Hubbard interaction strength (U=1.70eV). The projected DOS (blue line) between the Hubbard-like bands originate from the Dirac cone states within the graphene layer d) Measured STS of G/1T-TaS_2 qualitatively agrees with the calculated result in (c), displaying Hubbard-like peaks, with a gap size that is reduced with respect to the Mott gap observed in bare 1T-TaS_2, and mid-gap states which we associate with the graphene layer. Spectra in (b),(d) are taken at a set point of [V_b=1.2V, I_{SP}=80pA] with AC modulation $V_{AC} = 8mV$. Lower and upper Hubbard peaks are highlighted in blue and violet, respectively.

Next, we compare the calculated DOS with measured STS (proportional to the local DOS) on both the bare 1T-TaS_2 [Fig. 3(a),(b)] and graphene covered regions (Fig. 3c,d). GGA+U DOS of bare 1T-TaS_2 shown in Fig. 3(a) reflect the key features of the 1T-TaS_2 band structure in Fig. 2(a). The lower and upper Hubbard bands located respectively below E_F and ~0.35 eV above E_F with a ~0.35 eV Mott gap in between. The dips below LHB and above UHB indicate the scale of the CDW gap [Fig. S6]. These main features are consistent with those observed in our STS measurement [shown in Fig. 3(b)] which also show the expected Mott gap at the Fermi level flanked by lower and upper Hubbard peaks at -256mV and 144mV, respectively. Additionally, the two large dI/dV dips observed at -378mV and 218 mV are associated with the known CDW gap.

With graphene on top of 1T-TaS_2, the GGA+U DOS plotted in Fig. 3(c) also show UHB, LHB, Mott gap, and CDW gap similar to the DOS of bare 1T-TaS_2. The main differences from the bare 1T-TaS_2 case are i) the relative energies of the Fermi level, UHB, LHB, and Dirac point; ii) the linearly dispersing states within the Mott gap. Owing to the relatively stronger electron negativity of TaS_2, there exist notable charge transfer from graphene to 1T-TaS_2. Consequently, the Fermi level moves from the LHB top to the UHB bottom, meanwhile the graphene Dirac point shifts to a higher energy about 0.3eV above E_F. On the other hand, the mid-gap linear band comes from the Dirac cone states of the graphene cover layer. Because of the energy shift of the Dirac point to ~0.3eV above E_F, the V-shape DOS thus moves to ~0.3eV, leaving a linear-like band within the Mott gap below E_F.

The main features given from GGA+U are in good agreement with our STS results shown in Fig. 3(d). Two peaks near the Fermi level are labelled as lower and upper Hubbard bands (measured at -280mV and 88mV, respectively) with a V shaped DOS in between. Unlike the case of pristine, undoped graphene on an insulating substrate, here the DOS does not vanish at the Fermi level. The negative slope of the measured STS in between the Hubbard bands suggests the Dirac point in graphene has shifted to higher energies, indicative of the hole doping. We note that the GGA+U calculation of the DOS [Fig. 3(c)] is averaged over the entire heterostructure whereas the measured STS favors the region closest to the tip [Fig. 3(d)]. The preferential tunneling into the graphene top layer results in a larger mid-gap STS intensity (compared to Hubbard peak heights) than given by the calculation. Further modelling is needed to reproduce the relative spectral weights due to different orbitals within the vdW heterostructure as measured by an STM tip above the surface.

Comparing STS measurements of bare 1T-TaS_2 [Fig. 3(b)] and G/TaS_2 [Fig. 3(d)], we can see that the addition of the graphene layer induces both a shift of the Hubbard peaks as well as a reduction of the gap between them by approximately 7.5%. We interpret the reduction of the Mott gap size as being due to screening of the Coulomb interaction near the surface of 1T-TaS_2 by itinerant electrons in graphene, reducing U and the separation between Hubbard peaks. As mentioned above, we adopt a smaller on-site U=1.70eV in the calculation of the G/TaS_2 case to consider this screening effect observed in STS.

We note that taking a unit cell consisting of two layers of 1T-TaS_2 results in dimerization between layers, as suggested by recent theoretical and experimental works [32-35]. In this case, 1T-TaS_2 is no longer best described as a two-dimensional Mott insulator with magnetic ordering, but rather a band insulator, as the formation of interlayer dimer singlets suppresses magnetism. We show in Supplemental Material [Fig. S7] that the main features of adding a graphene layer on top of one or two layers of 1T-TaS_2 are qualitatively similar to the single layer case, giving rise to a shift of E_F, reducing the gap size, and featuring charge transfer with the graphene layer. Our experimental technique is not sensitive to the spin-polarization; thus, we cannot identify the magnetic ground state of 1T-TaS_2 in this study. However, our calculations suggest that if a magnetic moment is present in 1T-TaS_2, the addition of the graphene layer will not suppress the moment at the surface. Therefore, measurements using graphene encapsulation and spin-polarized STM tips might be able to identify the magnetic properties of the 1T-TaS_2 surface in future measurements.

As mentioned above, the charge density map in Fig. 1(c) left panel shows the hole density in graphene induced by 1T-TaS_2, which corresponds to the local charge transfer from graphene to TaS_2. The missing electron density in graphene shows a clear correlation with the CDW pattern in 1T-TaS_2, indicating a proximity-induced CDW in graphene. Figure 2(e) demonstrates the real-space interlayer hybridization arising from the state around the Dirac-LHB crossing points in reciprocal space. The interlayer charge density overlap indicates that the graphene and 1T-TaS_2 layers are intimately connected by tunneling electrons, resulting in a novel proximity effect induced by charge transfer as discussed below.

To gain more physical insight to the CDW proximity effect at a microscopic level, in particular the mechanism for charge transfer between the two layers and how it leads to CDW on the graphene layer via proximity effect from the CDW on1T-TaS2 layer, we construct a simple mean-field model Hamiltonian to complement our experimental observations and the first principle calculations. Therein, we assume a weak electron tunneling between the two layers since they are in close proximity to each other. The CDW on the graphene layer is then induced by the already-existing CDW on the 1T-TaS2 layer via the second-order electron hopping process between the two layers. We further analytically demonstrate that the particle-like CDW density observed on the 1T-TaS2 layer becomes the hole-like CDW density on the graphene layer due to this second-order electron hopping process

The simplified Hamiltonian of the G/TaS_2 bilayer system is given by:

$$H = H_d + H_c + H_t,$$

$$H_d = \sum_{\langle i,j\rangle,\sigma} -t_{ij}^{d} d_{i,\sigma}^{\dagger} d_{j,\sigma} + h.c. - \sum_{\langle i',j'\rangle,\sigma} (\Delta_d^{CDW}(i',j'))^{*} d_{i',\sigma}^{\dagger} d_{j',\sigma} + h.c. + \sum_{\langle i',j'\rangle} \left|\Delta_d^{CDW}(i',j')\right|^2,$$

$$H_c = \sum_{\langle i,j\rangle,\sigma} -t_{ij}^{c} c_{i,\sigma}^{\dagger} c_{j,\sigma} + h.c. = \sum_{k,\sigma} (\epsilon_k - \mu) c_{k,\sigma}^{\dagger} c_{k,\sigma},$$

$$H_t = -t \sum_{i,\sigma} c_{i,\sigma}^{\dagger} d_{i,\sigma} + h.c.,$$

where H_d (H_c) stands for the simplified Hamiltonian of the 1T-TaS_2 (graphene) layer, respectively, and H_t describes a weak charge transfer (hopping) term between these two layers (we neglect a small mismatch in spatial locations between the nearest-neighbor sites of the corresponding layer). The insulating 1T-TaS_2 layer shows CDW order with the order parameter $\Delta_d^{CDW}(i',j') \equiv \sum_\sigma \langle d_{i',\sigma}^{\dagger} d_{j',\sigma} \rangle$ where i', j' are sites within the CDW unit cell. The graphene layer has the linear Dirac dispersion: $(\epsilon_k - \mu) \approx \hbar v_F |k - k_F|$. Here, i, j refer to the nearest-neighbor sites of the corresponding lattices, and $t_{ij}^{d(c)}$ refers to the nearest-neighbor tight-binding hoping terms on the 1T-TaS_2 (graphene) layer, respectively.

Via the second order perturbation in the H_t term of the CDW unit cell, the following exchange term $H_t^{(2)}$ is generated:

$$H_t^{(2)} = t^2 \sum_{\langle i',j'\rangle,\sigma,\sigma'} c_{i',\sigma}^{\dagger} d_{i',\sigma} d_{j',\sigma'}^{\dagger} c_{j',\sigma'} + h.c.$$

A simple mean-field decoupling of $H_t^{(2)}$ in terms of $\Delta_d^{CDW}(i',j')$ (considering only $\sigma = \sigma'$ and assuming spin-isotropic CDW order $\langle d_{j',\uparrow}^{\dagger} d_{j',\uparrow} \rangle = \langle d_{j',\downarrow}^{\dagger} d_{j',\downarrow} \rangle$) gives $H_t^{(2)} \to H_{t^2}^{MF}$ with:

$$H_{t^2}^{MF} \approx -t^2/2 \sum_{\langle i',j'\rangle,\sigma} (\Delta_d^{CDW}(i',j'))^* c_{i',\sigma}^{\dagger} c_{j',\sigma} - t^2/2 \sum_{\langle i',j'\rangle,\sigma} (\Delta_d^{CDW}(i',j'))^* \langle c_{i',\sigma}^{\dagger} c_{j',\sigma} \rangle + h.c.,$$

where the mean-field decoupling term ($\langle c_{i',\sigma}^{\dagger} c_{j',\sigma} \rangle d_{i',\sigma}^{\dagger} d_{j',\sigma}$) in $H_t^{(2)}$ is neglected since we expect $\left|\langle c_{i',\sigma}^{\dagger} c_{j',\sigma} \rangle\right| \ll \left|\langle d_{i',\sigma}^{\dagger} d_{j',\sigma} \rangle\right|$. The CDW proximity effect is manifested in $H_{t^2}^{MF}$ as a weak CDW order $\sum_\sigma \langle c_{i',\sigma}^{\dagger} c_{j',\sigma} \rangle$ is induced on the graphene layer by the second order charge transfer between the two layers with the following identification:

$$\Delta_c^{CDW}(i',j') \equiv -1/2 \sum\nolimits_\sigma \langle c_{i',\sigma}^{\dagger} c_{j',\sigma} \rangle^* = -t^2/2 \left(\Delta_d^{CDW}(i',j')\right)^*,$$

or equivalently, $\sum_\sigma \langle c_{i',\sigma}^{\dagger} c_{j',\sigma} \rangle = t^2 \Delta_d^{CDW}(i',j')$. Via the above identification, the Hamiltonian $H_{t^2}^{MF}$ can be expressed as:

$$H_{t^2}^{MF} = \sum_{\langle i',j'\rangle,\sigma} \Delta_c^{CDW}(i',j') c_{i',\sigma}^{\dagger} c_{j',\sigma} + h.c. + 2|\Delta_c^{CDW}(i',j')|^2,$$

which leads to $\Delta_c^{CDW}(i',j') = -1/2 \sum_\sigma \langle c_{i',\sigma}^{\dagger} c_{j',\sigma} \rangle^*$ identified above via minimizing the free energy associated with $H_{t^2}^{MF}$ with respect to $\Delta_c^{CDW}(i',j')$. Note that from above derivations, we indeed find

that $\left|\langle c^{\dagger}_{i',\sigma} c_{j',\sigma}\rangle\right| \sim t^2 \left|\langle d^{\dagger}_{i',\sigma} d_{j',\sigma}\rangle\right| \ll \left|\langle d^{\dagger}_{i',\sigma} d_{j',\sigma}\rangle\right|$, as expected. Note also that the CDW order parameters induced on graphene layer shows the opposite sign with respect to that on 1T-TaS_2 layer, consistent with the hole-like (particle-like) CDW intensity on graphene (1T-TaS_2) layer obtained from DFT calculations, respectively. We emphasize here that the above mechanism based on charge transfer is distinct from all the previously realized proximity effects, including superconducting, magnetic and spin-orbit proximity effects.

In summary, we demonstrate, by STM/STS measurements and DFT calculations, the existence of a novel proximity-induced CDW in graphene resulting from the short-range exchange interaction with the CDW hosted by the 1T-TaS_2 crystal. Concomitant with the proximity induced CDW in graphene, which is out-of-phase with that in 1T-TaS_2, we observe a substantial reduction in the Mott gap of the 1T-TaS_2 crystal, indicating the presence of proximity-induced mid-gap carriers which screen the Mott-Hubbard interaction. These observations open intriguing possibilities for engineering correlations and manipulating charge carriers in heterostructures. They provide a new platform for non-linear electronic devices based on sliding, pinning, and phonon softening of the CDW induced within the graphene layer. Additional measurements including spin-resolved STM/STS, Raman spectroscopy, and electronic transport will further help elucidate the effects proposed in this work.

Methods: Samples were fabricated by mechanical exfoliation of graphene and separately TaS_2 flakes inside an argon-filled glovebox. The thin TaS_2 flake (2.4-24nm or 4-40 layers) was exfoliated from a bulk 1T-TaS_2 crystal, which was grown by iodine chemical vapor transport, and transferred onto a passivated SiO_2-capped degenerately doped Si wafer. The graphene and 1T-TaS_2 flakes were aligned vertically and brought into close contact with micromanipulators under an optical microscope and then heated to promote adhesion. Standard electron beam lithography and electrode deposition (4-5nm Ti/40-50nm Au) were used to make electrical contact to the sample [36]. After removing the PMMA mask the resulting heterostructure was annealed (180-220°C) in hydrogen/argon (10%/90%) to remove polymer residues [37]. STM and STS were performed using a homebuilt STM [38-40] at 78K in high-vacuum $<10^{-5}$ Torr. At this temperature we partially remove the encapsulating graphene layer using the STM tip (mechanically cut Pt/Ir) resulting in a region that allows us to differentiate the properties of bare and graphene covered 1T-TaS_2 (see Supplementary Figure S1). We use an RHK R9 SPM controller for electronic control and data acquisition.

Acknowledgements

MAA was supported by the National Science Foundation grant EFRI 1433307; EYA and NT acknowledge support from the Department of Energy grant DOE-FG02-99ER45742 and the Gordon and Betty Moore Foundation EPiQS initiative grant GBMF9453; GL was supported by Rutgers University; CJW was supported by The National Research Foundation of Korea (NRF), grant No. 2016K1A4A4A01922028 and 2020M3H4A2084417; SWC was supported by the Betty Moore Foundation's EPiQS grant GBMF6402 and Rutgers University, C.-H. C. was supported by MOST (Grant NO.: 107-2112-M-009-010-MY3, 110-2112-M-A49-018-MY3) and the NCTS of Taiwan, R.O.C., J.H.T acknowledges support from the Ministry of Science and Technology, Taiwan under grant: MOST 109-2112-M-007 -034 -MY3, and from NCHC, CINC-NTU, AS-iMATE-109-13, and CQT-NTHU-MOE, Taiwan.

1 Geim, A. K. & Grigorieva, I. V. Van der Waals heterostructures. *Nature* **499**, 419-425, doi:10.1038/nature12385 (2013).

2 Levy, N. *et al.* Strain-Induced Pseudo-Magnetic Fields Greater Than 300 Tesla in Graphene Nanobubbles. *Science* **329**, 544-547 (2010).

3 Carrillo-Bastos, R. *et al.* Strained fold-assisted transport in graphene systems. *Physical Review B* **94**, 125422, doi:10.1103/PhysRevB.94.125422 (2016).

4 Jinhai Mao, S. P. M., Miša Anđelković, Xinyuan Lai, & Yang Cao, K. W., Takashi Taniguchi, Lucian Covaci, Francois M. Peeters, Andre K. Geim. Yuhang Jiang, Eva Y. Andrei. Evidence of Flat Bands and Correlated States in Buckled Graphene Superlattices. *Nature* **584** (2020).

5 Meissner, H. Superconductivity of Contacts with Interposed Barriers. *Physical Review* **117**, 672-680, doi:10.1103/PhysRev.117.672 (1960).

6 Hauser, J. J. Magnetic Proximity Effect. *Physical Review* **187**, 580-583, doi:10.1103/PhysRev.187.580 (1969).

7 Zhao, R. *et al.* Tuning Phase Transitions in 1T-TaS2 via the Substrate. *Nano Letters* **17**, 3471-3477, doi:10.1021/acs.nanolett.7b00418 (2017).

8 Frano, A. *et al.* Long-range charge-density-wave proximity effect at cuprate/manganate interfaces. *Nature Materials* **15**, 831-834, doi:10.1038/nmat4682 (2016).

9 Li, A. J., Zhu, X., Stewart, G. R. & Hebard, A. F. Bi-2212/1T-TaS2 Van der Waals junctions: Interplay of proximity induced high-Tcsuperconductivity and CDW order. *Scientific Reports* **7**, 4639, doi:10.1038/s41598-017-04645-1 (2017).

10 Dreher, P. *et al.* Proximity Effects on the Charge Density Wave Order and Superconductivity in Single-Layer NbSe2. *ACS Nano*, doi:10.1021/acsnano.1c06012 (2021).

11 Du, X., Skachko, I. & Andrei, E. Y. Josephson current and multiple Andreev reflections in graphene SNS junctions. *Phys. Rev B* **77** (2008).

12 Heersche, H. B., Jarillo-Herrero, P., Oostinga, J. B., Vandersypen, L. M. K. & Morpurgo, A. F. Bipolar supercurrent in graphene. *Nature* **446**, 56-59, doi:10.1038/nature05555 (2007).

13 Avsar, A. *et al.* Spin-orbit proximity effect in graphene. *Nat Commun* **5**, 4875, doi:10.1038/ncomms5875 (2014).

14 Liang, X. *et al.* The magnetic proximity effect and electrical field tunable valley degeneracy in MoS2/EuS van der Waals heterojunctions. *Nanoscale* **9**, 9502-9509, doi:10.1039/c7nr03317f (2017).

15 Heersche, H. B., Jarillo-Herrero, P., Oostinga, J. B., Vandersypen, L. M. & Morpurgo, A. F. Bipolar supercurrent in graphene. *Nature* **446**, 56-59, doi:10.1038/nature05555 (2007).

16 Keimer, B., Kivelson, S. A., Norman, M. R., Uchida, S. & Zaanen, J. From quantum matter to high-temperature superconductivity in copper oxides. *Nature* **518**, 179-186, doi:10.1038/nature14165 (2015).

17 Lin, D. *et al.* Patterns and driving forces of dimensionality-dependent charge density waves in 2H-type transition metal dichalcogenides. *Nat Commun* **11**, 2406, doi:10.1038/s41467-020-15715-w (2020).

18 Burk, B., Thomson, R. E., Zettl, A. & Clarke, J. Charge-density-wave domains in 1T-TaS2 observed by satellite structure in scanning-tunneling-microscopy images. *Phys Rev Lett* **66**, 3040-3043, doi:10.1103/PhysRevLett.66.3040 (1991).

19 Thomson, R. E., Burk, B., Zettl, A. & Clarke, J. Scanning tunneling microscopy of the charge-density-wave structure in 1T-${\mathrm{TaS}}_{2}$. *Physical Review B* **49**, 16899-16916, doi:10.1103/PhysRevB.49.16899 (1994).

20 Altvater, M. *et al.* Electrostatic imaging of encapsulated graphene. *2D Materials*, doi:10.1088/2053-1583/ab254e (2019).
21 Ramos, S. L. L. M. *et al.* Suppression of the commensurate charge density wave phase in ultrathin 1T-TaS2 evidenced by Raman hyperspectral analysis. *Physical Review B* **100**, 165414, doi:10.1103/PhysRevB.100.165414 (2019).
22 Altvater, M. A. *et al.* Observation of a topological defect lattice in the charge density wave of 1T-TaS2. *Applied Physics Letters* **119**, 121601, doi:10.1063/5.0059662 (2021).
23 Chen, C., Singh, B., Lin, H. & Pereira, V. M. Reproduction of the Charge Density Wave Phase Diagram in 1T-$TiSe_2$ Exposes its Excitonic Character. *Physical Review Letters* **121**, 226602, doi:10.1103/PhysRevLett.121.226602 (2018).
24 Zhang, K. *et al.* Evidence for a Quasi-One-Dimensional Charge Density Wave in CuTe by Angle-Resolved Photoemission Spectroscopy. *Physical Review Letters* **121**, 206402, doi:10.1103/PhysRevLett.121.206402 (2018).
25 Kresse, G. & Furthmüller, J. Efficiency of ab-initio total energy calculations for metals and semiconductors using a plane-wave basis set. *Computational Materials Science* **6**, 15-50, doi:https://doi.org/10.1016/0927-0256(96)00008-0 (1996).
26 Kresse, G. Ab initio molecular dynamics for liquid metals. *Journal of Non-Crystalline Solids* **192-193**, 222-229, doi:https://doi.org/10.1016/0022-3093(95)00355-X (1995).
27 Kresse, G. & Furthmüller, J. Efficient iterative schemes for ab initio total-energy calculations using a plane-wave basis set. *Physical Review B* **54**, 11169-11186, doi:10.1103/PhysRevB.54.11169 (1996).
28 Perdew, J. P. *et al.* Atoms, molecules, solids, and surfaces: Applications of the generalized gradient approximation for exchange and correlation. *Physical Review B* **46**, 6671-6687, doi:10.1103/PhysRevB.46.6671 (1992).
29 Perdew, J. P. & Wang, Y. Pair-distribution function and its coupling-constant average for the spin-polarized electron gas. *Physical Review B* **46**, 12947-12954, doi:10.1103/PhysRevB.46.12947 (1992).
30 Darancet, P., Millis, A. J. & Marianetti, C. A. Three-dimensional metallic and two-dimensional insulating behavior in octahedral tantalum dichalcogenides. *Physical Review B* **90**, 045134, doi:10.1103/PhysRevB.90.045134 (2014).
31 Qiao, S. *et al.* Mottness Collapse in 1T−TaS2−xSex Transition-Metal Dichalcogenide: An Interplay between Localized and Itinerant Orbitals. *Physical Review X* **7**, 041054, doi:10.1103/PhysRevX.7.041054 (2017).
32 Ngankeu, A. S. *et al.* Quasi-one-dimensional metallic band dispersion in the commensurate charge density wave of 1T-TaS_2. *Physical Review B* **96**, 195147, doi:10.1103/PhysRevB.96.195147 (2017).
33 Ritschel, T., Berger, H. & Geck, J. Stacking-driven gap formation in layered 1T-TaS2. *Physical Review B* **98**, 195134, doi:10.1103/PhysRevB.98.195134 (2018).
34 Lee, S. H., Goh, J. S. & Cho, D. Origin of the Insulating Phase and First-Order Metal-Insulator Transition in 1T-TaS_2. *Phys Rev Lett* **122**, 106404, doi:10.1103/PhysRevLett.122.106404 (2019).
35 Butler, C. J., Yoshida, M., Hanaguri, T. & Iwasa, Y. Mottness versus unit-cell doubling as the driver of the insulating state in 1T-TaS2. *Nat Commun* **11**, 2477, doi:10.1038/s41467-020-16132-9 (2020).
36 Luican-Mayer, A. *et al.* Negative differential resistance observed on the charge density wave of a transition metal dichalcogenide. *Nanoscale* **11**, 22351-22358, doi:10.1039/c9nr07857f (2019).
37 Wang, Z. *et al.* Surface-Limited Superconducting Phase Transition on 1 T-TaS2. *ACS Nano* **12**, 12619-12628, doi:10.1021/acsnano.8b07379 (2018).

38 Li, G., Luican, A. & Andrei, E. Y. Scanning Tunneling Spectroscopy of Graphene on Graphite. *Physical Review Letters* **102**, 176804, doi:10.1103/PhysRevLett.102.176804 (2009).
39 Li, G., Luican, A. & Andrei, E. Y. Self-navigation of a scanning tunneling microscope tip toward a micron-sized graphene sample. *Review of Scientific Instruments* **82**, 073701, doi:10.1063/1.3605664 (2011).
40 Li, G., Luican-Mayer, A., Abanin, D., Levitov, L. & Andrei, E. Y. Evolution of Landau levels into edge states in graphene. *Nat Commun* **4**, 1744, doi:10.1038/ncomms2767 (2013).

Supporting Information

Revealing the Charge Density Wave Proximity Effect in Graphene on 1T-TaS_2

Michael A. Altvater[1], Sheng-Hsiung Hung[2], Nikhil Tilak[1], Choong-Jae Won[3], Guohong Li[1], Sang-Wook Cheong[1], Chung-Hou Chung[4], Horng-Tay Jeng[2] and Eva Y. Andrei[1]*

Removing Graphene with STM Tip

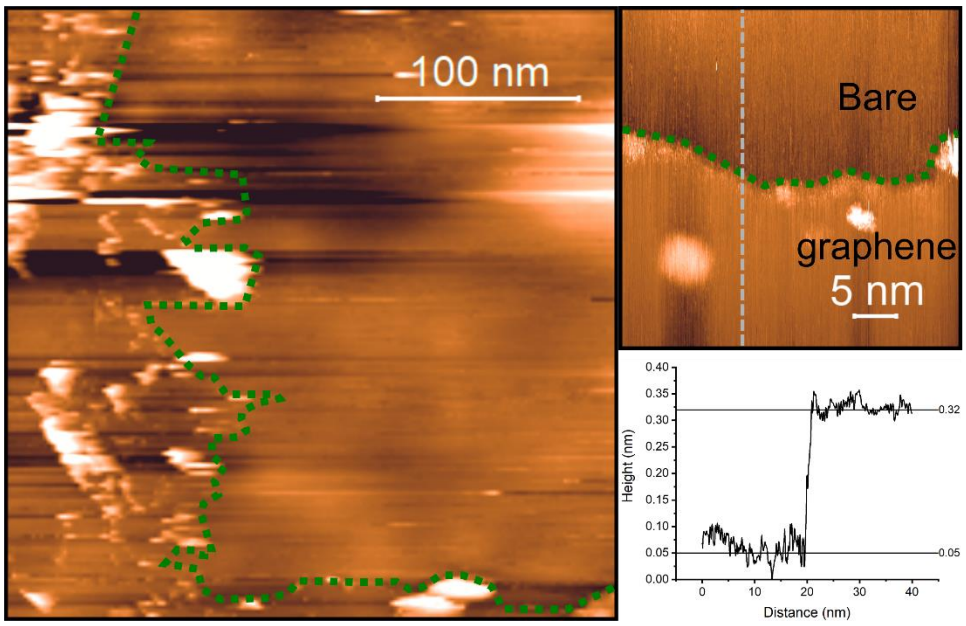

Figure S1: a) Large area topography image at the corner where graphene has been removed from the TaS_2 surface. Edge of graphene is outlined with a green, dashed line. b) Zoomed in image of the graphene edge, highlighted with a green, dashed line. c) Linecut along the gray dashed line in (b) showing a step across the graphene edge showing a 0.27±0.07 nm step

We find that for low biases and large set currents (when the tip is near the surface), the graphene layer is able to be lifted by the STM tip. This tip-graphene interaction allows us to peel a region of graphene off of the 1T-TaS_2 surface at 77K, exposing a region of bare 1T-TaS_2.

Moiré Pattern Between Graphene and TaS_2

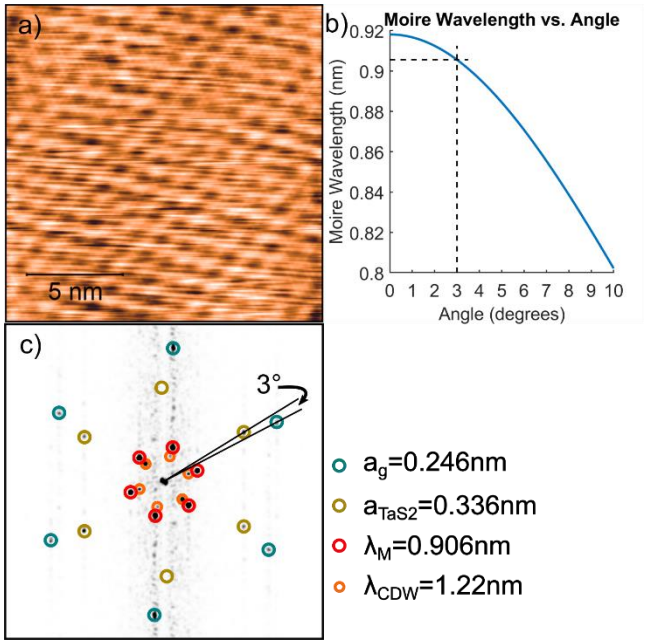

Figure S2: a) STM topography displaying a Moiré interference pattern as well as charge density wave modulation (V_b=0.550V, I_{SP}=150pA) b) Plot of the expected Moiré pattern wavelength between the graphene and TaS_2 lattices as a function of angle. The experimentally determined value is marked with dashed lines c) Fourier transform of the topography image in (a) shows peaks associated with the graphene lattice ($a_g = 0.246nm$ is assumed), 1T-TaS_2 lattice (measured $a_{TaS2} = 0.336nm$), the induced Moiré wavelength (measured $\lambda_M = 0.906nm$), and the commensurate CDW (measured $\lambda_{CDW} = 1.22nm$)

In a different region of the structure and at a different bias voltage than shown in the main text, we more clearly resolve the graphene and TaS_2 lattices [Figure S2(a)]. The structure observed is different than that of the previous region [figure 1, main text]. The differences can be identified more clearly by viewing the FFT of the real space image [Figure S2(c)]. In the Fourier transform we can find 4 sets of Bragg peaks with different wavevectors. For accuracy, we compare the measured wavevectors to that of the graphene lattice [the outermost set of peaks in figure S2(c)]. We find that the other 3 sets of peaks correspond to the periodic modulations of the TaS_2 lattice ($a_{TaS2} = 0.336nm$), the commensurate charge density wave ($\lambda_{CDW} = 1.22nm$), as well as a modulation with period $\lambda = 0.906nm$. It is known that interference between two misaligned periodic patterns leads to a Moiré superpattern, observable by STM. The well-known relationship between the Moiré period and the crystal lattice mismatch is given by:

$$\lambda_M = \frac{(1+\delta)a_g}{\sqrt{2(1+\delta)(1-\cos\theta)+\delta^2}}$$

For the lattice mismatch between the graphene and TaS_2 lattice, $\delta = \frac{a_{TaS2}}{a_g} - 1 \approx 0.366$, the Moiré wavelength as a function of angle is plotted at low angles in Figure 5(b). We can use the positions of the Bragg peaks associated with crystalline lattices to determine the angle between graphene and TaS_2 in this region to be approximately $\theta = 3°$. Thus, we identify the unknown periodic modulation as the Moiré pattern induced by interference between the graphene and TaS_2 lattices.

Kohn Anomalies and CDW Supercell

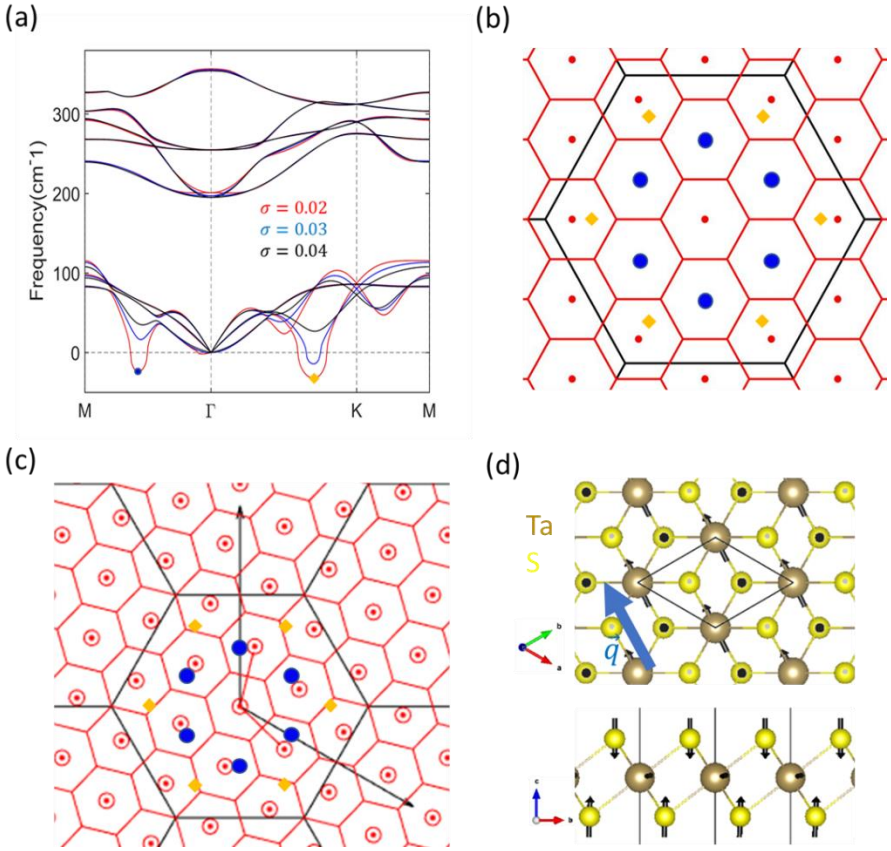

Figure S3: a) Phonon dispersion of undistorted 1T-TaS_2. The Kohn anomaly wavevectors are marked by blue circle and yellow rhombus. Different broadening values σ indicate the temperature effect. b) Kohn anomaly wavevectors and Brillouin zone (BZ) of 1×1 (black) and $\sqrt{13} \times \sqrt{13}$ (red) structures. The blue Kohn anomaly wavevector **q** along ΓM locates at the zone centers of the $\sqrt{13} \times \sqrt{13}$ CDW BZs, whereas the yellow Kohn anomaly wavevector along ΓK does not fit the $\sqrt{13} \times \sqrt{13}$ CDW BZs. (c) The $\sqrt{13} \times \sqrt{13}$ CDW BZs are rotated to form the commensurate BZs. d) Ta atoms vibrate parallel to the Kohn anomaly wavevector **q**, while S atoms vibrate perpendicularly to **q**.

The calculated phonon dispersion for the unreconstructed 1T-TaS_2 in Fig. S3(a) shows two Kohn anomalies, phonon modes whose frequencies drop to (or below) zero, indicating a lattice instability. These Kohn anomalies can be stabilized without negative frequency by using higher broadening (σ) values. This corresponds to the removed CDW phase at higher temperatures observed in experiments.

The blue Kohn anomaly instability at wavevector **q** coincides with the wavevector $\mathbf{Q_{CDW}}$ of the $\sqrt{13} \times \sqrt{13}$ CDW reconstruction, suggesting electron-phonon coupling as a possible origin for the CDW. Fig. S3(b) demonstrates that the blue Kohn anomaly wavevector **q** along ΓM locates at the zone centers of the $\sqrt{13} \times \sqrt{13}$ CDW BZs. The good match in the periodicity indicates the tendency from 1x1 unit cell toward the $\sqrt{13} \times \sqrt{13}$ CDW lattice. Although the q vector of 1x1 unit cell matches the period of $\sqrt{13} \times \sqrt{13}$ BZ, it is not possible for the 1x1 BZ to match the non-integer $\sqrt{13} \times \sqrt{13}$ BZ. This actually suggests a ~13.9° rotation of the $\sqrt{13} \times \sqrt{13}$ BZ as shown in Fig. S3(c). The rotated $\sqrt{13} \times \sqrt{13}$ supercell thus commensurate with the 1x1 unit cell as observed and discussed in this work experimentally and theoretically. On the other hand, the yellow Kohn anomaly does not fit the BZ of possible minimum supercells and thus is not observed. The blue soft phonon mode at the Kohn anomaly wavevector **q** contains mainly longitudinal vibration of Ta atoms with minor transverse vibration of S atoms relative to the phonon propagating direction **q** as depicted in Fig. S3(d).

CDW Induced Isolated Flat Band

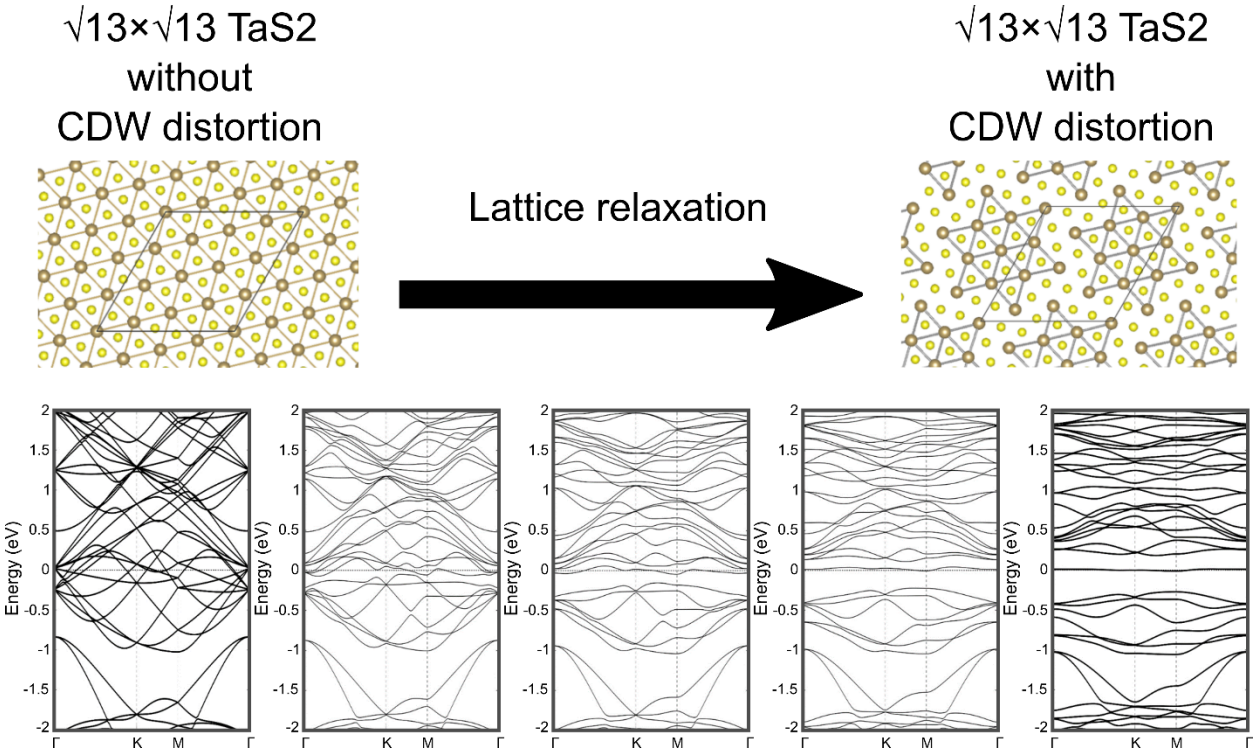

Figure S4: Evolution of the GGA band structure (bottom) as the lattice relaxes (from left to right) from the undistorted lattice structure (shown top, left) to the $\sqrt{13} \times \sqrt{13}$ distortion (top, right)

The undistorted 13 Ta atoms within the $\sqrt{13} \times \sqrt{13}$ supercell (top-left panel), the same size as the CDW unit cell (top-right panel), each contribute one conduction electron to the undistorted band structure (bottom-left panel). As the lattice is allowed to relax, 6 of these Ta-associated bands are pushed below the Fermi level while 6 are pushed to higher energies, leaving a single, flat, isolated band at the Fermi level (bottom-right panel). This band is associated with an electron state localized at the

center of the Stars of David in the CDW reconstructed structure (top-right panel). As a flat, isolated band, the electronic kinetic energy (and kinetic energy spread) is low, allowing interparticle interactions to dominate and correlated electronic phases can emerge.

Hubbard U Enhanced Gap

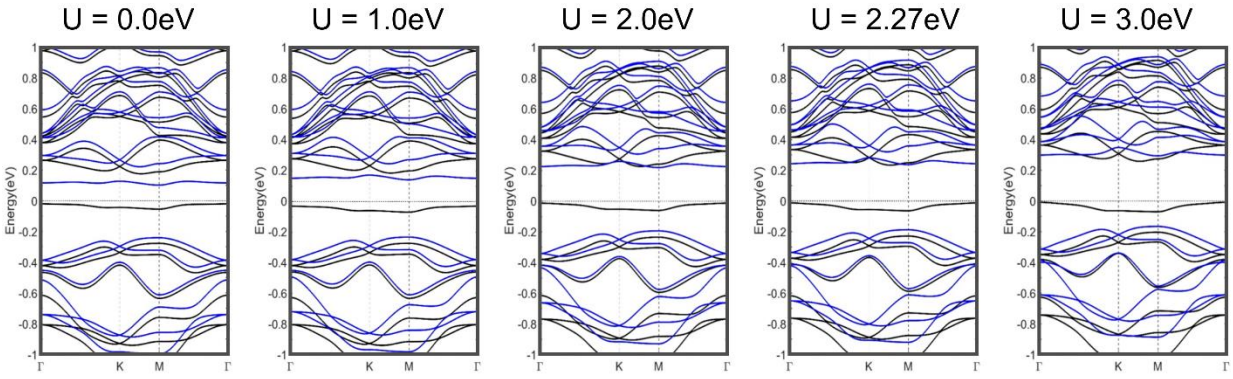

Figure S5: Evolution of the GGA+U band structure with increasing values of Hubbard U from 0 to 3 eV.

In the 1T-TaS_2 monolayer, the DFT calculation shows an exchange gap at the Fermi level, even without including a Hubbard U. However, this gap is much smaller than that measured experimentally. To reproduce experimental observations, a Hubbard U is added to the calculation to encompass Coulomb repulsion between electrons in neighboring CDW stars. Increasing the value of U enhances the gap at the Fermi level. The value of U=2.27eV, previously determined from linear response theory, is used in the calculations given in the main text.

CDW, Exchange, and Mott gaps

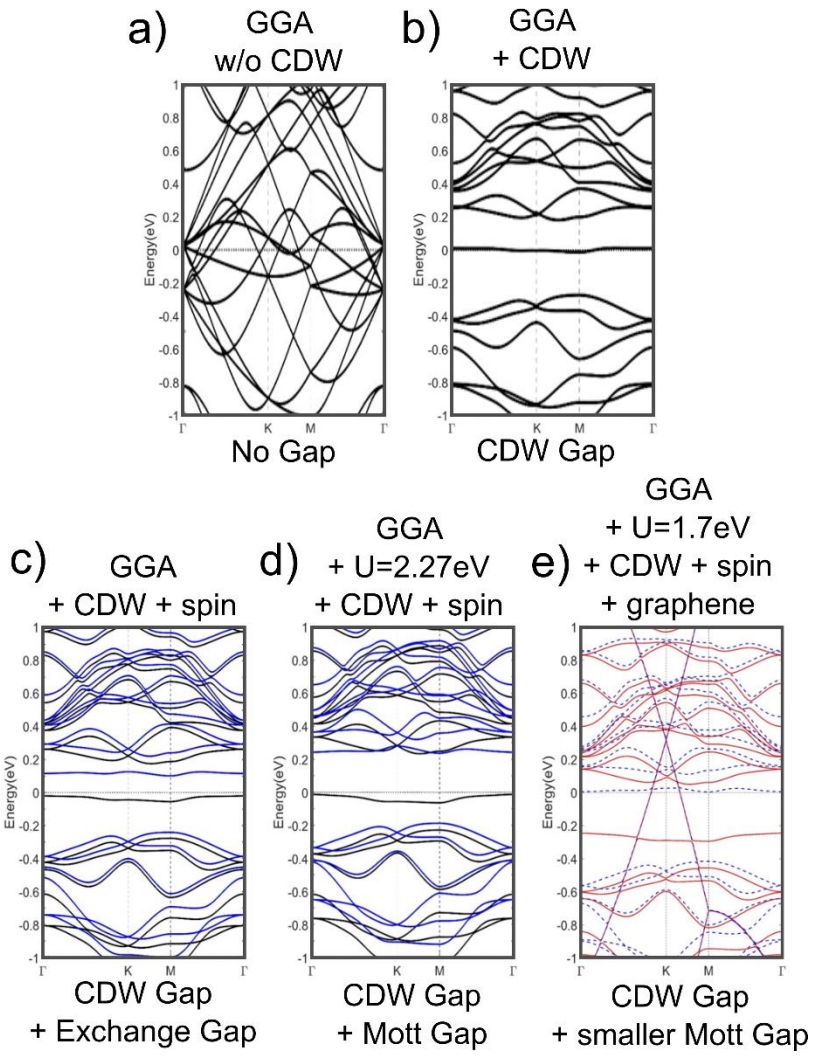

Figure S6: a) GGA band structure of undistorted 1T-TaS_2 shows no band gap. b) After relaxing the lattice, a CDW gap opens with an in-gap, half-filled, isolated flat band stuck at E_F. c) Adding spin splits the isolated flat band into two spin-polarized bands separated by an exchange gap. d) Increasing the on-site Hubbard U expands the exchange gap into the experimentally observed Mott gap. e) With the addition of graphene, the Hubbard U and the associated Mott gap are reduced in size due to screening from the graphene layer.

The outline of the emergence of the insulating state of 1T-TaS_2 begins with the CDW lattice reconstruction which isolates a narrow, flat band at the Fermi level within the CDW-induced gap. Including spin freedom and exchange interactions, the flat band splits into an exchange gap at the Fermi level. Adding a Hubbard U, enhances the gap into a Mott gap which reproduces experimental observations. Finally, adding a graphene layer on top causes a shift of the 1T-TaS_2 bands toward lower energies and adds a Dirac cone, centered at the K-points of the superstructure Brillouin zone. Additionally, the graphene layer is found to reduce the spacing between the Upper and Lower Hubbard bands of 1T-TaS_2 which is captured by using a smaller value of Hubbard U=1.70eV.

Bilayer 1T-TaS_2

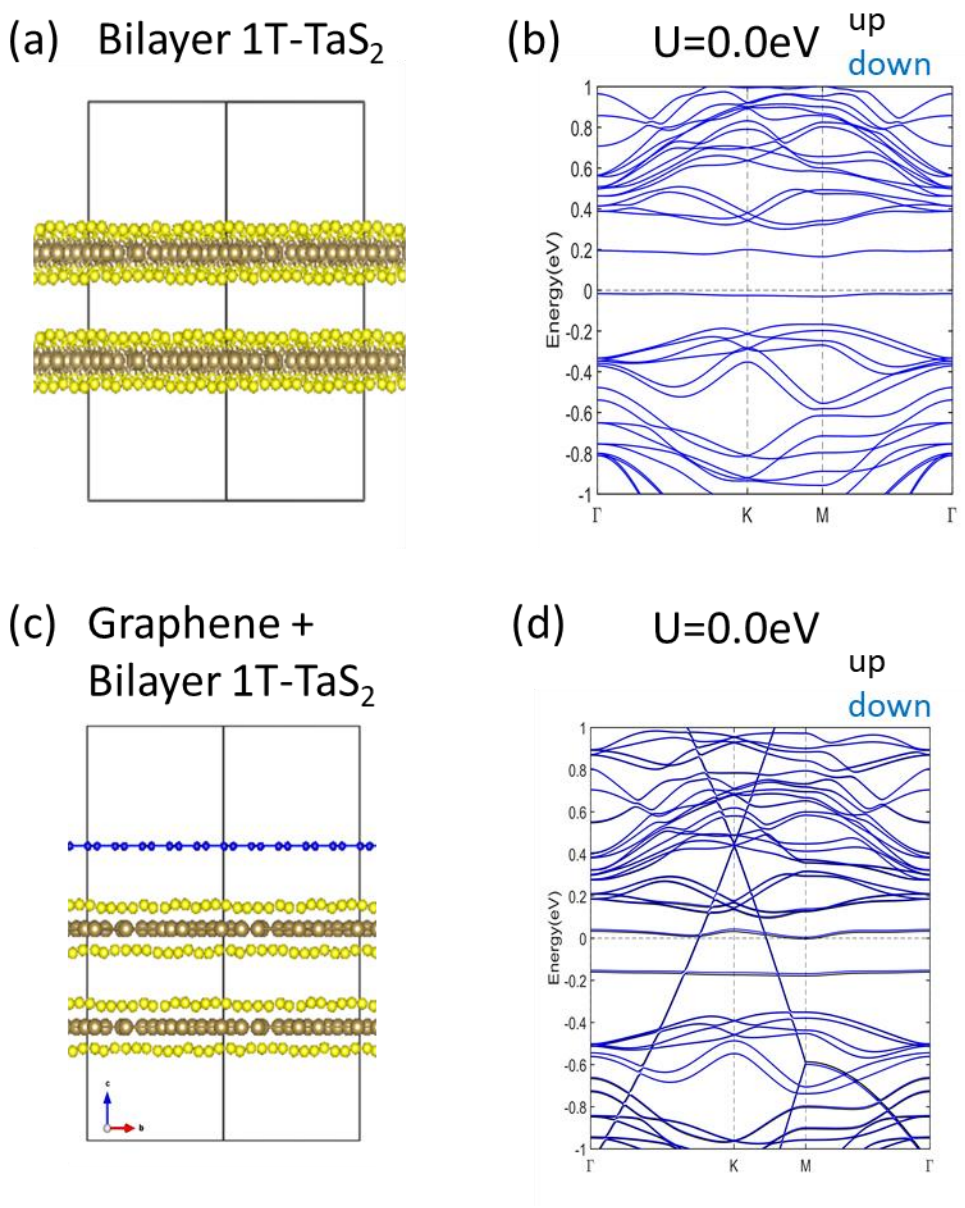

Figure S7: a) Ball and stick model of the unit cell used in the bilayer 1T-TaS_2 calculation with CDW clusters aligned along the c-axis. b) Calculated band structure of bilayer 1T-TaS_2 gives band insulating behavior as interlayer dimerization forms occupied and unoccupied bonding and anti-bonding states with no net magnetic moment. c) Ball and stick model of the unit cell used to calculate the band structure of graphene on bilayer 1T-TaS_2. 5x5 unit cells of graphene are placed on top of the bilayer 1T-TaS_2 structure used in (a). d) Band structure of the G/ bilayer 1T-TaS_2 heterostructure shows that the flat bands of the bilayer 1T-TaS_2 and the Dirac cone of graphene are preserved in the heterostructure as well as a ~7.7% reduction of the spacing between flat bands with the addition of graphene.

We firstly calculated the total energies for different stacking configurations of 1T-TaS2 bilayer with van der Waals interaction included. Our calculations conclude that the AA stacking is more stable in

dimerized bilayer 1T-TaS2. Another related calculation for bulk 1T-TaS2 can be found in [14]. Next, we use the AA stacking bilayer 1T-TaS_2 with Graphene on top as our lattice model and calculate the band structure. The flat band from each single layer 1T-TaS_2 is in the ferromagnetic state. The two ferromagnetic states of the bilayer rearrange their spins into the antiparallel singlet state as the two layers are dimerized. Hence, bilayer TaS2 has no total magnetic moment. Adding graphene to bilayer 1T-TaS_2 has similar effect as the monolayer 1T-TaS_2 case. First, charge transfer from Graphene to 1T-TaS_2 shifts the Dirac cone above fermi level [Fig. S7(d)]. The charge transfer corresponds to hole doping in graphene and shows charge modulations with the same pattern as the start-shape CDW of 1T-TaS_2. Second, the charge transfer also causes the reduction of the gap between two flat bands [Figs. S7(b,d)].